Interstitial hydrogen diffusion in M_7C_3 (M = Cr, Mn, Fe),

Krause, Andreas; Olsson, Pär; Music, Denis; Bjerkén, Christina

Published in:
Computational Materials Science

DOI:
10.1016/j.commatsci.2022.111940

2023

Document Version:
Publisher's PDF, also known as Version of record

Computational Materials Science 218 (2023) 111940

Contents lists available at ScienceDirect

Computational Materials Science

journal homepage: www.elsevier.com/locate/commatsci

Full length article

Interstitial diffusion of hydrogen in M_7C_3 (M=Cr,Mn,Fe)

Andreas M. Krause [a,*], Pär A.T. Olsson [a,b], Denis Music [a], Christina Bjerkén [a]

[a] Department of Materials Science and Applied Mathematics, Malmö University, SE-211 19 Malmö, Sweden
[b] Division of Mechanics, Lund University, Box 118, SE-221 00 Lund, Sweden

ARTICLE INFO

Keywords:
Hydrogen embrittlement
Hydrogen diffusion
Carbides
Density functional theory
Nudged elastic band method

ABSTRACT

To increase the understanding of the role of carbide precipitates on the hydrogen embrittlement of martensitic steels, we have performed a density functional theory study on the solution energies and energy barriers for hydrogen diffusion in orthorhombic M_7C_3 (M = Cr, Mn, Fe). Hydrogen can easily diffuse into the lattice and cause internal stresses or bond weakening, which may promote reduced ductility. Solution energies of hydrogen at different lattice positions have systematically been explored, and the lowest values are -0.28, 0.00, and 0.03 eV/H-atom for Cr_7C_3, Mn_7C_3, and Fe_7C_3, respectively. Energy barriers for the diffusion of hydrogen atoms have been probed with the nudged elastic band method, which shows comparably low barriers for transport via interstitial octahedral sites for all three systems. Analysis of the atomic volume reveals a correlation between low solution energies and energy barriers and atoms with large atomic volumes. Furthermore, it shows that the presence of carbon tends to increase the energy barrier. Our results can explain previous experimental findings of hydrogen located in the bulk of Cr_7C_3 precipitates and provide a solid basis for future design efforts of steels with high strength and commensurable ductility.

1. Introduction

Hydrogen has for quite some time been discussed as a possible fuel in a low carbon-emission society [1]. Not only related to hydrogen storage tanks, but even in other applications where an abundance of hydrogen comes in close contact with engineering materials, hydrogen may cause premature failure due to hydrogen embrittlement [2]. The lack of understanding of the underlying mechanisms behind hydrogen embrittlement has made it an active field of research for more than two decades. Owing to its small size and generally high mobility, hydrogen can easily penetrate metal lattices and dissolve in most metals and alloys [2–4]. It can be conceived as either diffusible hydrogen, which can easily move through interstitial lattice sites, or trapped hydrogen, thereby usually residing around imperfections in the crystal that serve as trapping sites, e.g., vacancies, dislocations, grain boundaries, and interfaces [5–8]. Diffusible and trapped hydrogen can even be found in precipitates [9]. Following adsorption at the surface, hydrogen can readily diffuse through the lattice [10] and even recombine to form molecular hydrogen at defect sites, such as grain boundaries or voids [11]. Even the formation of hydrides can occur in some alloys [12,13]. Such disruptions in the lattice can promote unwanted side effects like decreased yield and ultimate tensile strengths, reduced ductility, as well as lowered fatigue strength. Moreover, aspects such as stress corrosion cracking, delayed hydride cracking, or other hydrogen-related fracture mechanisms can lead to reduced load-carrying capability and, ultimately, catastrophic failure [2,11,13].

Due to the importance of engineering steels, there is a particular focus on hydrogen embrittlement therein [2,11,14,15]. There exist both experimental and theoretical studies on hydrogen trapping and diffusion in ferrite (bcc), austenite (fcc), and the carbide cementite (Fe_3C) [2,14,16,17]. However, little is known about other carbides that form, especially in non-equilibrium systems like martensite [18]. One family of carbides forming in chromium steels during tempering are M_7C_3-carbides, with M = Cr, Mn, or Fe [19,20]. These carbides have the same structure for all three elements, with an orthorhombic *Pnma* symmetry [21–23], and they commonly form at the interface between ferrite and M_3C in a nano-scale size [9,24].

Hydrogen is mostly found at the interface between ferrite and M_7C_3. But, investigations of hydrogen distribution in chromium carbides with high-resolution tritium micro-autoradiography have shown that hydrogen was not only found in the boundary proximity of carbide inclusions but also inside [25], which raised the question whether chromium carbides can trap hydrogen. Similar observations were made with atom probe tomography, which showed evidence for hydrogen inside the carbide, not just at the boundary [10]. A mass spectrum analysis even confirmed that only individual hydrogen atoms, i.e. not molecular hydrogen, were segregated within the chromium carbide [10].

* Corresponding author.
E-mail address: andreas.krause@mau.se (A.M. Krause).

https://doi.org/10.1016/j.commatsci.2022.111940
Received 23 February 2022; Received in revised form 17 November 2022; Accepted 25 November 2022

Table 1
Dependence of the solution energy at an octahedral site in Cr_7C_3 as a function of supercell size. All energies are in eV/H-atom.

	1 × 1 × 1	1 × 2 × 1	1 × 3 × 1	2 × 1 × 1	3 × 1 × 1
ΔE_{Sol}	−0.246	−0.253	−0.261	−0.244	−0.251

Investigations by Lee et al. [9] have suggested that M_7C_3 may act as hydrogen-trapping sites. However, these experimental studies do not provide any data about hydrogen trap site strength or the energy demand for hydrogen migration through carbides.

This study aims to investigate the solution energies and energy barriers, associated with hydrogen diffusion through bulk M_7C_3, using density functional theory (DFT). The observed solution energies and energy barriers for bulk diffusion are rationalized by geometric and electronic structure analysis, which yields a sound basis for improving the understanding of hydrogen embrittlement of state-of-the-art nanostructured alloys.

2. Computational method

Plane-wave DFT calculations were performed using the Vienna Ab-initio Simulation Package (VASP) [26–28]. Periodic boundary conditions were applied as well as spin polarization to account for magnetism (ferromagnetic ordering). The generalized gradient approximation was used to describe the exchange correlation functional by applying the Perdew–Burke–Ernzerhof (PBE) scheme [29] for all simulations. We adopted a cut-off energy of 520 eV and a convergence criterion for the total energy of 10^{-4} eV. Initial Cr_7C_3, Mn_7C_3, and Fe_7C_3 configurations were taken from The Materials Project database [30] and were subsequently relaxed with respect to both coordinates and lattice parameters. For the carbide unit cell, a Monkhorst–Pack [31] k-point mesh of $12 \times 8 \times 4$ was used. For supercell calculations, the k-point grid was adjusted such that the k-point density matched that of the unit cell.

Size convergence of the supercell was checked to avoid interaction of hydrogen with its periodic image and to estimate the interaction energy. Following the procedure in [14], the solution energy of a hydrogen atom at an octahedral site in supercells comprising different multiples of the Cr_7C_3 unit cell was computed. The energy convergence was estimated by comparing the energy difference between consecutively increased supercell sizes. The results shown in Table 1 reveal that a $2 \times 1 \times 1$ supercell size yields a deviation in the order of 14 meV/H-atom, which is of sufficient accuracy for the present investigation.

Consistent with previous works [18], we use hydrogen in ferrite (bcc-Fe) as a reference for the calculation of the solution energy in the carbides. For this purpose, we computed the energy of a $3 \times 3 \times 3$ bcc-Fe supercell containing 54 iron atoms without and with one hydrogen atom at a tetrahedral site following the method presented in [32]. The solution energy is then defined as:

$$\Delta E_{sol} = (E_{wH} - E_{w/oH}) - (E_{Fe_{wH}} - E_{Fe_{w/oH}}), \quad (1)$$

where E_{wH} is the energy associated with the carbide supercell that contains one hydrogen atom, while $E_{w/oH}$ is that of the carbide supercell without any hydrogen. Likewise, $E_{Fe_{wH}}$ is the total energy of a bcc-Fe cell with hydrogen, while $E_{Fe_{w/oH}}$ is that without hydrogen.

The solution energy correction arising from quantum mechanical zero-point vibrations has been calculated for all systems containing hydrogen, including the bcc-Fe structure. For this purpose, the metal and carbon atoms were kept fixed, while the hydrogen atom was perturbed in each direction by 0.015 Å and the vibrational frequencies were calculated. The zero-point energy (ZPE) was then approximated as

$$ZPE = \frac{1}{2}\sum_i \hbar v_i, \quad (2)$$

Table 2
Calculated lattice parameters (a, b, c) compared with the experimental data from the literature in brackets.

	Cr_7C_3	Cr_7C_3	Fe_7C_3
a [Å]	4.506 (4.526)[a]	4.461 (4.541)[b]	4.517 (4.540)[c]
b [Å]	6.945 (7.010)[a]	6.945 (7.010)[b]	6.857 (6.879)[c]
c [Å]	12.038 (12.142)[a]	11.701 (11.988)[b]	11.762 (11.942)[c]

[a]Ref. [49].
[b]Ref. [23].
[c]Ref. [48].

where $\hbar$ is Planck's constant (divided by 2π) and v_i are the computed normal vibration frequencies.

To identify saddle points and extract energy barriers associated with hydrogen diffusion, calculations using the nudged elastic band (NEB) method [33–36] were performed. Between two nearby metastable hydrogen solution sites, a string of eight images was created on a direct line with a spring constant of 5 eV/Å^2 between the consecutive images. Since linear interpolation was used to generate the image structures, each structure was initially inspected to avoid initial hydrogen positions in too close proximity to the neighboring lattice atoms. In the case that unreasonably high energies were obtained for any of the images, the hydrogen atom was displaced to a nearby site, and the NEB calculations were restarted from the new position.

Treatment of H diffusivity in some solids (e.g. Fe and Pd) below room temperature may require the employment of classical transition state theory with quantum corrections to capture the effects of H tunneling [37,38]. In the present work, we opted to ignore such quantum effects for three reasons: (i) Acceptable agreement between experimental and classically computed data for H diffusion in several metals has been previously reported in the literature [39], (ii) Cr_7C_3 is characterized by a generally high Debye temperature – of the order of 730 K [40] – while H tunneling is expected primarily for systems with the Debye temperature below 350 K [41], and finally (iii) the quantum effects are either negligible in many systems, such as Ni [37], TiAl [42], VC, TiC, NbC, TaC [43], and Mo with additions of 3d, 4d, and 5d transition metals [44], or contribute up to 15% of the total binding energy [45], rendering them insensitive to the general trends in H diffusion.

For the electronic analysis, the density of states (DOS) was computed using single-point calculations with a convergence criterion of 10^{-6} eV for the total energy. The VESTA software package was used for visualizations on the atomic scale [46] and the OVITO software package [47] was employed for the Voronoi analysis.

3. Results and discussion

3.1. Lattice structure, geometry, and atomic volume

The obtained equilibrium lattice constants at 0 K for the three carbides are given in Table 2. They underestimate the experimental data by between 0.4% and 2.4% [23,48,49], which is an acceptable deviation based on the PBE exchange–correlation functional used herein [50]. Similar underestimation of the lattice constants in M_7C_3 carbides has been reported previously [40,51,52] in which PBE was used. Analysis of magnetic properties reveals that Cr_7C_3 and Mn_7C_3 are non-magnetic, and Fe_7C_3 is ferromagnetic with a magnetic moment on each Fe atom of about 1.72 μ_B, which agrees well with earlier studies [52–54]. Hence, the structural and spin polarization data imply that the hydrogen-free configurations of these three carbides are described with an acceptable precision.

To identify plausible interstitial sites, a visual inspection of the cell has been performed first to estimate the volume of individual sites. The sites of interest were not limited to those with tetrahedral or octahedral coordination, but also other sites were considered. Each

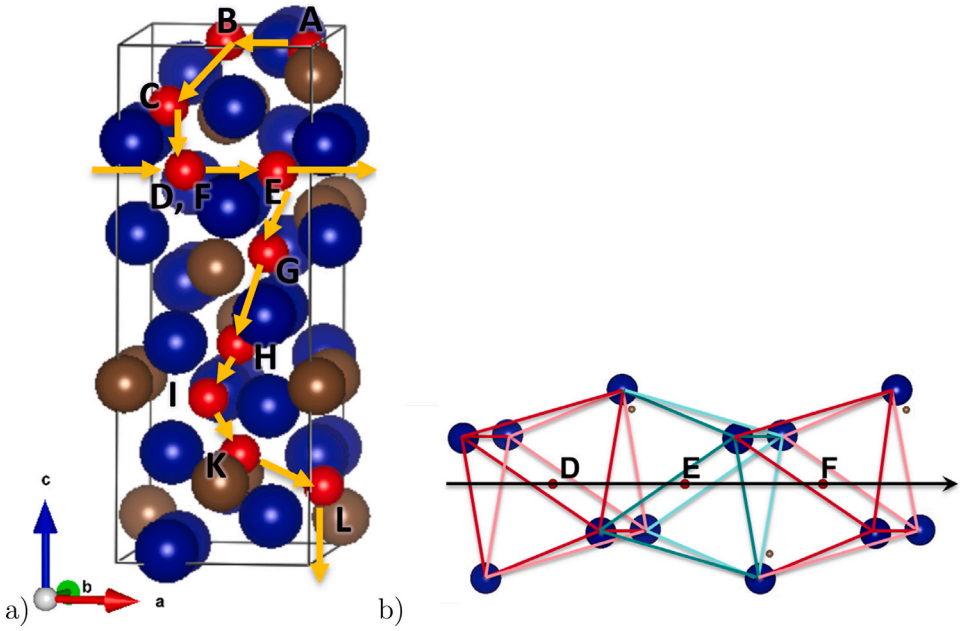

Fig. 1. (a) M_7C_3 simulation cell with interstitial hydrogen positions—colored red and labeled A–L. Carbon atoms are in brown, chromium atoms in blue. The suggested diffusion paths are marked with orange arrows and are identical for all three carbides; (b) Magnification of the octahedral sites in the positions D, E, and F. As a guide to the eye, the octahedral sites were framed with red/light red and green/light green bars. The blue spheres in the corners are metal atoms, and the small red dots in the center of the octahedral site are hydrogen positions. The black arrow indicates the direction chosen for the NEB calculations.

position was checked for its equivalent position within the *Pnma* space group. Possible diffusion paths between the sites were chosen based on the following criteria: (i) volume estimate of the site, (ii) the area estimate of the site's face through which diffusion has to take place, and (iii) the distance to other atoms along the possible diffusion path.

The identified possible interstitial hydrogen sites in M_7C_3 can be seen in Fig. 1a labeled A–L. Identified interstitial diffusion pathways in the *a*- and in *c*-directions are indicated by the arrows, where the *a*-direction contains positions D–E–F, and *c*-direction positions A–L without position F. As the adopted supercell is the double unit cell size in the *a*-direction, position F is a periodic replica of position D. The symmetry of the structure reveals that possible diffusion pathways along the *b*-direction is through symmetric images of segregation sites that are already part of the diffusion pathways in the *a*- and *c*-directions. Thus, diffusion in the *b*-direction is expected to have solution energies and energy barriers that are in a range of those found in the *a*- and *c*-directions. Therefore, the *b*-direction has not been considered further in this study. Due to the apparently large volume of sites along the *a*-direction (Fig. 1b) the pathway between the positions D–E–F appears to be a plausible diffusion trajectory.

To correlate the site geometry with the segregation preference, we performed a Voronoi analysis, see Fig. 2. Following coordinate relaxation, we found that the hydrogen atoms were preferentially located at the intersections of the Voronoi surfaces, i.e., on points/lines between two adjacent atoms. The most favorable positions are octahedral interstitial sites (OS) that are surrounded by metal atoms. The metal atoms in the corner of the OS are associated with 5% larger atomic volumes than the metal atoms at other sites, which suggests that there is more space for hydrogen to reside. The volume of the OS for the positions D, E, and F in Cr_7C_3, Mn_7C_3, and Fe_7C_3 was calculated to be 8.62, 7.97, and 8.25 $Å^3$, respectively. The volume associated with the carbon atoms was found to be only 28% of that for the metal atoms. Position K is in a trigonal bipyramidal site with three metal atoms with low volume situated at the corners of the bipyramid's base plane and two carbon atoms at the top edges. Due to the smaller atomic volumes of the carbon atoms, there is less space for a hydrogen atom to fit in that site, which implies an energy penalty. Thus, the closer a hydrogen atom comes to the carbon atoms, the more unfavorable the segregation site becomes.

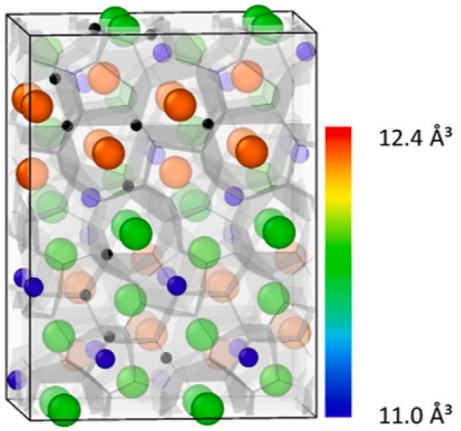

Fig. 2. The Voronoi analysis of Cr_7C_3. The color scale is from small atomic volumes (blue) to large atomic volumes (red). Hydrogen atoms (black) are located at the edges of Voronoi polyhedron (gray). The metal atoms in the corners of the octahedral site have 5% larger volumes than metal atoms in the rest of the system. Atomic volumes of carbon atoms are below the lower barrier of the scale and therefore depicted in dark blue.

Such a repulsive effect between C and H interstitial atoms in steel has already been reported by Timmerscheidt et al. [54].

3.2. Solution energies and energy barriers

As hydrogen is the lightest element, the quantum mechanical zero-point vibrations and the associated ZPE are particularly important to describe the solution energy. For hydrogen dissolved in Cr_7C_3, Mn_7C_3, and Fe_7C_3, it corresponds to 0.21, 0.17, and 0.19 eV/H-atom, respectively. The ZPE for the hydrogen atom in bcc-Fe has been calculated to be 0.23 eV/H-atom, which is in agreement with earlier calculations [55, 56].

The ZPE-corrected solution energies calculated relative to hydrogen in bcc-Fe for all positions are provided in Table 3. The total range of the

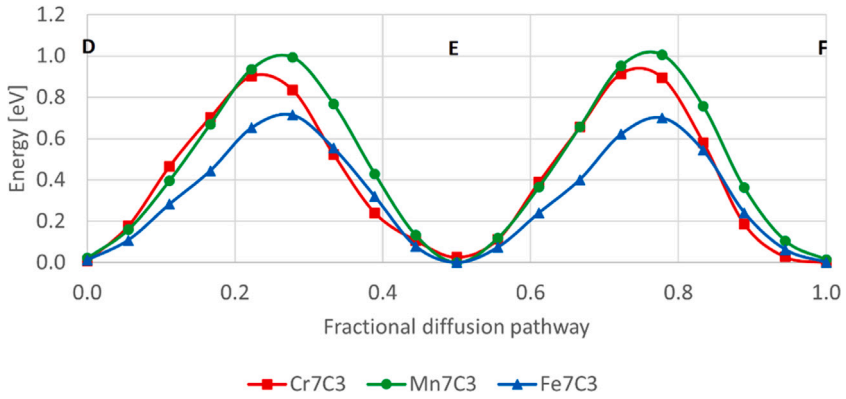

Fig. 3. Energy profile for the diffusion of hydrogen in the *a*-direction, calculated with the NEB method using linear interpolations between the minima. The *x*-axis shows the investigated diffusion pathway through the positions D–E–F as indicated in Fig. 1.

Table 3
ZPE corrected solution energies for hydrogen at the positions A–L in M_7C_3. The solution energies are relative to the solution energy of hydrogen in bcc-Fe. V_H is the atomic volume of hydrogen in the respective solution site in Cr_7C_3.

Position	V_H [Å^3]	Solution energies [eV/H-atom]		
	in Cr_7C_3	Cr_7C_3	Mn_7C_3	Fe_7C_3
A	1.02	1.34	1.14	1.23
B	1.09	0.55	0.32	0.94
C	1.12	1.11	1.14	1.07
D	1.35	−0.28	0.00	0.04
E	1.34	−0.27	0.02	0.03
F	1.35	−0.28	0.00	0.04
G	1.16	1.12	1.17	1.12
H	0.84	0.75	0.45	0.42
I	1.01	0.67	0.34	0.26
K	0.99	1.49	1.49	1.30
L	1.01	0.47	0.35	0.21

solution energies for all three systems is up to 1.77 eV/H-atom, with general trends similar for all considered carbides. For the investigated positions, some sites in the *c*-direction show much higher solution energies than the sites in the *a*-direction. The most endothermic solution energy of hydrogen in Cr_7C_3 is found at position K, which has a 1.77 eV/H-atom higher energy than the corresponding lowest solution energy (position D/F). Comparing the solution energies and the atomic volume of interstitial hydrogen (see Table 3) implies that the sites with the largest volume exhibit the lowest solution energy, and vice versa. The influence of carbon on the solution energy, as already touched upon in Section 3.1 and further discussed in Section 3.3, is apparent. For the other two carbides, the energy difference between the highest and lowest solution energy is less than in the case of Cr_7C_3 (Mn_7C_3 1.49 eV/H-atom, Fe_7C_3 1.30 eV/H-atom). For Cr_7C_3 solution energies with a minimum of −0.28 eV/H-atom relative to hydrogen in bcc-Fe could be observed, indicating that the OS at the positions D, E, and F are weakly stable positions for hydrogen. This also suggests that Cr_7C_3 is more prone to uptake of hydrogen than Fe_7C_3 and Mn_7C_3. This is consistent with calculations done by Salehin et al. [18] and the fact that Cr_7C_3 is often argued to have a weak hydrogen trapping tendency in steel [9,10,25].

As we were interested in the energy barriers for hydrogen diffusion in M_7C_3, we employed the NEB method to calculate the energy barriers along sequences of interstitial sites (see Fig. 1). Along the *a*-direction, the pathway through the OS at positions D–E–F was analyzed (see Fig. 3) and in the *c*-direction, a path A–L (without point F, see Fig. 4) was considered. The energy barrier for both transitions D–E and E–F is nearly identical within each system, reaching 0.98, 1.03, and 0.72 eV for Cr_7C_3, Mn_7C_3, and Fe_7C_3, respectively. Thus, in the case of Fe_7C_3, the calculated energy barrier is more than 0.2 eV lower than for the other two carbides considered herein.

The energy barriers in the *c*-direction of the carbides are given in Fig. 4. The maximum values are 3.39, 3.21, and 2.73 eV for Cr_7C_3, Mn_7C_3, and Fe_7C_3, respectively. Thus, the experienced energy barriers for hydrogen moving in the *c*-direction are up to three times higher than in the *a*-direction. Again, we find that the energy barriers are the lowest in the case of Fe_7C_3. We note remarkably high energy barriers for the transitions from positions K–L and G–H in Cr_7C_3 with 3.47 and 3.37 eV, respectively, relative to the lowest energy point, point E, in the energy profile.

To investigate the electronic influence on the solution energies, in addition to the volumetric analysis, we performed an electronic structure analysis by calculating the DOS. We considered both the total and the partial DOS for hydrogen. Therefore, spin-polarized single-point calculations for Cr_7C_3 were performed for the configuration with the lowest solute energy (point E), the highest solute energy (point K) and the saddle-point with the highest energy (between K and L), according to the designation depicted in Fig. 4. Fig. 5 shows the corresponding total DOS and partial DOS for hydrogen. While the total DOS data seem to be only mildly affected by the position of hydrogen in the lattice, hydrogen 1s states are quite sensitive. The states attributed to the H-1s at point E are shifted by 0.2 eV to higher energies compared to the saddle-point data, which indicates a less favorable electronic structure at the maximum between K and L (saddle point). The DOS for point K is distributed within an energy range covered by DOS of the low solute-energy-point E and the saddle point. This suggests that changes in the solution energies are not only related to geometric factors but also to unfavorable changes in the electronic structure.

3.3. Influence of carbon on the solution energies at the octahedral sites

The lowest hydrogen solution energies are found at octahedrally coordinated sites. As it can be seen in Fig. 6, these OS have only metal atoms positioned in their corners as the nearest neighbor atoms to a hydrogen atom. In a second coordination shell around the OS, there are carbon atoms as the next nearest neighbor atoms. To investigate the extent to which solution energies are affected by the local chemical environment, i.e., carbon atoms, we compare the OS in Fe_7C_3 (Fe_7C_3-OS) with the similarly shaped OS found in fcc-Fe (fcc-Fe-OS). Differences in the energy barriers and solution energies between these two systems are discussed based on inherent geometric and electronic factors.

The fcc-Fe-OS is known to be a stable hydrogen solution site [14]. For the comparison between the two OS, we performed calculations on fcc-Fe with and without hydrogen in the same manner as Ismer et al. [14]. For better comparability, we recalculated the energies for the fcc-Fe-OS and the Fe_7C_3-OS according to [14], gaining energies of 0.20 and 0.30 eV/H-atom, respectively. The energy barriers for the diffusion of hydrogen through the face of the OS are 0.62 eV/H-atom

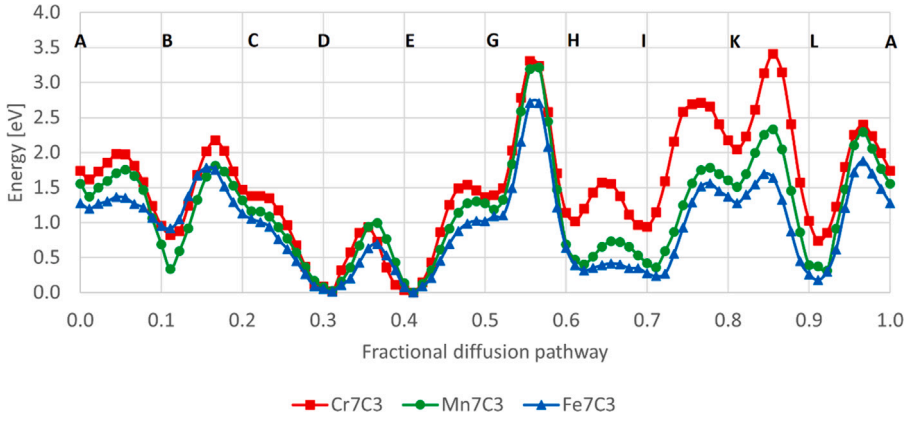

Fig. 4. Energy barrier for the diffusion of hydrogen in the *c*-direction, calculated with the NEB method using linear interpolations between the minima. Calculations have been performed for all three systems Cr_7C_3, Mn_7C_3 and Fe_7C_3. The *x*-axis shows the investigated diffusion pathway through the positions A to L (without F).

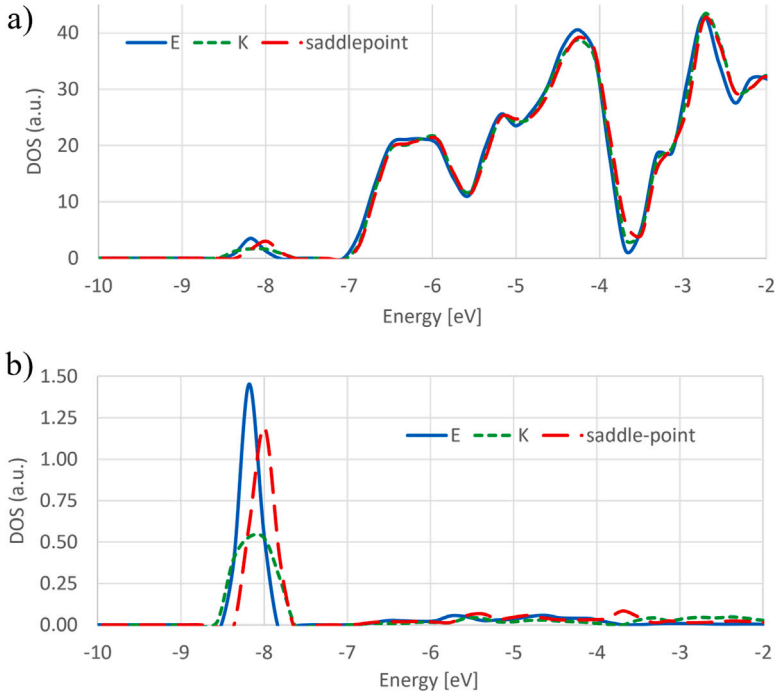

Fig. 5. DOS for low energy configuration E (blue), configuration K (green) and the saddle-point between K and L (red) energy in Cr_7C_3. Total DOS is shown in (a), while the partial DOS for hydrogen is given in (b). The energy scale is shifted relative to the Fermi energy. Spin up and down states were summed up.

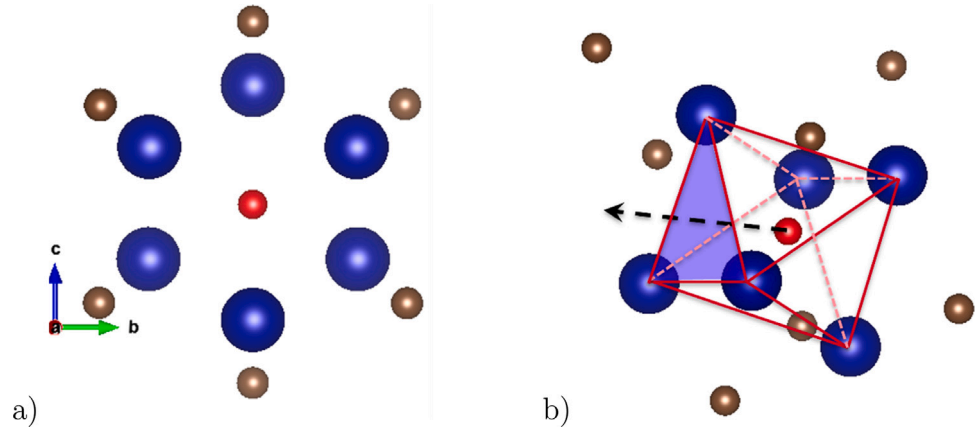

Fig. 6. Fe_7C_3-OS (a) in the direction of diffusion and (b) a rotated view to emphasize the OS with hydrogen in its center. First nearest neighbor atoms are Fe atoms (blue, large spheres), and next nearest neighbor atoms are carbon atoms (brown, small spheres). Red lines in (b) frame the OS. When diffusing in the *a*-direction (black arrow) hydrogen must penetrate through the blue face of the octahedron.

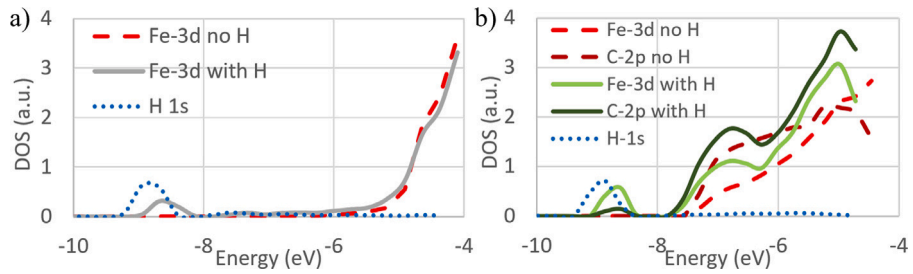

Fig. 7. DOS for the nearest neighboring atoms to an octahedral site in (a) fcc-Fe and (b) in Fe_7C_3. The overlap between the H-1s and the Fe-3d orbitals, which can be seen in both fcc-Fe and Fe_7C_3, is in the same energy range between −9.2 to −8.4 eV showing the same intensity. Overlap of the C-2p states in the same energy range exhibits a small intensity in the case of the carbide. The energy scale is shifted relative to the Fermi energy. Spin up and down states were summed up.

for the fcc-Fe-OS and 0.72 eV/H-atom for the Fe_7C_3-OS. The 0.1 eV/H-atom higher energy required to push a hydrogen atom through the face of the Fe_7C_3-OS correlates with a reduction of that face's area by 5.6% compared to the face of the fcc-OS, which has an area of 2.88 Å^2. The atomic volumes of the cornering Fe atoms are, with 11.86 Å^3, 2.1% smaller in the case of the Fe_7C_3-OS, explaining the 0.1 eV/H-atom higher solution energy in the case of the carbide. However, the Fe_7C_3-OS is, with a volume of 8.25 Å^3, 2.1% larger than the fcc-Fe-OS. These observations suggest that a larger volume of a site results in a lower solution energy and a more stable site. This raises the question whether there is an influence of the next nearest neighboring atoms, carbon atoms, on the solution energies of the carbide.

We considered the bonding of hydrogen at the OS and calculated the partial DOS for the nearest (metal corner atoms) and next nearest neighboring atoms (carbon atoms) of the Fe_7C_3-OS and compared them to the fcc-Fe-OS (see Fig. 7). In the carbide, hybridization between Fe-3d and C-2p orbitals occurs (Fig. 7b), which implies covalent bonding between Fe and C. This observation is in accordance with previous studies on Fe_7C_3 [52] and on the isostructural Cr_7C_3 system [51]. In Fig. 7a overlap between the H-1s and the Fe-3d states can be seen clearly for the fcc-Fe configuration. Fig. 7b shows the same overlap between the Fe-3d and H-1s states for Fe_7C_3. The overlap between Fe-3d and H-1s is found to be similar in terms of the energy range and the DOS in both cases, the pure metal and the carbide. Nevertheless, in Fig. 7b a minor increase in the DOS of the C-2p can be seen in the region between −9.2 to −8.4 eV, which overlaps with the Fe-3d and H-1s DOS, indicating an interaction of the C-2p with at least one of the other two orbitals. This can be interpreted as the cause for the slightly increased solution energy of H at the Fe_7C_3-OS. The combination of geometry analysis and overlap of electron states suggests that the solution energies of hydrogen at OS are dominated by the geometric arrangement. Still, there is a minor chemical component arising from the carbon atoms, the next nearest neighboring atoms. Although we limit this investigation to Fe_7C_3, we expect a similar trend in the other investigated carbides.

4. Conclusions

Our DFT study aims to shed some light on the role of bulk M_7C_3 for hydrogen trapping focusing on the corresponding solution energies and energy barriers. We have investigated hydrogen trapping and diffusion capabilities with DFT and kinetic energy barriers by employing NEB.

It is found that there is a negative solution energy for hydrogen in the interstitial octahedral site (−0.28 eV/H-atom) enabling Cr_7C_3 to act as a weak hydrogen trap. In contrast, the solution energies of hydrogen on the equivalent octahedral sites in Mn_7C_3 and Fe_7C_3 are 0.00 and 0.03 eV/H-atom. There is an energy barrier of 0.7–1.0 eV for hydrogen diffusion through the carbides via octahedral sites, which is the most favorable pathway in an otherwise rather anisotropic diffusion landscape. This may in parts be understood from the Voronoi analysis of the surrounding atoms of a site: Large atomic volumes contribute to lower solution energies and lower energy barriers. However, there is still a non-negligible chemical influence of close carbon atoms. Thus, the more carbon atoms along a possible diffusion pathway, the higher the energy barriers. Such argumentation is also corroborated by the electronic structure data. A comparison of octahedral-shaped sites in fcc-Fe and Fe_7C_3 has been done to determine the influence of next nearest neighboring atoms, carbon atoms, on the solution energies and shows that the solution energies of hydrogen at the OS are dominated by the geometry.

In this work, we have addressed only solution energies and energy barriers for hydrogen diffusion in ideal bulk M_7C_3 carbides. This constitutes the first approximation, which is a necessary step in acquiring the overall physical picture of hydrogen embrittlement of steels with M_7C_3 precipitations. An investigation of point defects, such as vacancies or anti-sites, is a topic to be addressed in the future. As is the interaction with the matrix (for instance, ferrite), which is also crucial for diffusion.

CRediT authorship contribution statement

Andreas M. Krause: Methodology, Validation, Formal analysis, Investigation, Data curation, Writing – original draft, Visualization. **Pär A.T. Olsson:** Conceptualization, Writing – review & editing. **Denis Music:** Conceptualization, Writing – review & editing. **Christina Bjerkén:** Conceptualization, Writing – review & editing, Project leader.

Declaration of competing interest

The authors declare that they have no known competing financial interests or personal relationships that could have appeared to influence the work reported in this paper.

Data availability

Data will be made available on request.

Acknowledgments

The computations were enabled by resources provided by the Swedish National Infrastructure for Computing (SNIC), partially funded by the Swedish Research Council through grant agreement no. 2018-05973. The presented work was a spin-off from the project HY-TOOLBOX (VINNOVA 2020-03115).

References

[1] G.W. Crabtree, M.S. Dresselhaus, M.V. Buchanan, The hydrogen economy, Phys. Today 57 (12) (2004) 39–44.
[2] O. Barrera, D. Bombac, Y. Chen, T.D. Daff, E. Galindo-Nava, P. Gong, D. Haley, R. Horton, I. Katzarov, J.R. Kermode, C. Liverani, M. Stopher, F. Sweeney, Understanding and mitigating hydrogen embrittlement of steels: a review of experimental, modelling and design progress from atomistic to continuum, J. Mater. Sci. 53 (9) (2018) 6251–6290.
[3] H. Hänninen, T. Hakkarainen, Fractographic characteristics of a hydrogen-charged AISI 316 type austenitic stainless steel, Metall. Trans. A 10 (8) (1979) 1196–1199.

[4] H. Wipf, Solubility and diffusion of hydrogen in pure metals and alloys, Phys. Scr. T 94 (1) (2001) 43.

[5] S.M. Myers, M.I. Baskes, H.K. Birnbaum, J.W. Corbett, G.G. DeLeo, S.K. Estreicher, E.E. Haller, P. Jena, N.M. Johnson, R. Kirchheim, S.J. Pearton, M.J. Stavola, Hydrogen interactions with defects in crystalline solids, Rev. Modern Phys. 64 (2) (1992) 559–617.

[6] G.M. Pressouyre, A classification of hydrogen traps in steel, Metall. Trans. A 10 (10) (1979) 1571–1573.

[7] G.M. Pressouyre, Hydrogen traps, repellers, and obstacles in steel; Consequences on hydrogen diffusion, solubility, and embrittlement, Metall. Trans. A 14 (10) (1983) 2189–2193.

[8] P.A.T. Olsson, K. Kese, A.-M. Alvarez Holston, On the role of hydrogen filled vacancies on the embrittlement of zirconium: An ab initio investigation, J. Nucl. Mater. 467 (2015) 311–319.

[9] J. Lee, T. Lee, D.-J. Mun, C.M. Bae, C.S. Lee, Comparative study on the effects of Cr, V, and Mo carbides for hydrogen-embrittlement resistance of tempered martensitic steel, Sci. Rep. 9 (1) (2019) 5219.

[10] X. Cheng, Z. Zhang, W. Liu, X. Wang, Direct observation of hydrogen-trapping sites in newly developed high-strength mooring chain steel by atom probe tomography, Prog. Nat. Sci. Mater. Int. 23 (4) (2013) 446–452.

[11] M. Nagumo, Hydrogen related failure of steels - a new aspect, Mater. Sci. Technol. 20 (8) (2004) 940–950.

[12] E. Tal-Gutelmacher, D. Eliezer, The hydrogen embrittlement of titanium-based alloys, JOM 57 (9) (2005) 46–49.

[13] M.P. Puls, The Effect of Hydrogen and Hydrides on the Integrity of Zirconium Alloy Components, first ed., Springer, London, 2012.

[14] L. Ismer, T. Hickel, J. Neugebauer, Ab initio study of the solubility and kinetics of hydrogen in austenitic high Mn steels, Phys. Rev. B 81 (9) (2010) 094111.

[15] R. Gibala, A.J. Kumnick, Hydrogen trapping in iron and steels, in: R. Gibala, R.F. Hehemann (Eds.), Hydrogen Embrittlement and Stress Corrosion Cracking, American Society for Metals (ASM), Cleveland, Ohio, 2002, pp. 61–78.

[16] A.S. Kholtobina, R. Pippan, L. Romaner, D. Scheiber, W. Ecker, V.I. Razumovskiy, Hydrogen trapping in bcc iron, Materials (Basel) 13 (10) (2020) 2288.

[17] D.A. Mirzaev, A.A. Mirzoev, K.Y. Okishev, A.V. Verkhovykh, Ab initio modelling of the interaction of H interstitials with grain boundaries in bcc Fe, Mol. Phys. 114 (9) (2016) 1502–1512.

[18] R. Salehin, G.B. Thompson, C.R. Weinberger, Hydrogen trapping and storage in the group IVB-VIB transition metal carbides, Mater. Des. 214 (2022) 110399.

[19] G.F. Vander Voort, G.M. Lucas, E.P. Manilova, Metallography and microstructures of stainless steels and maraging steels, in: G.F. Vander Voort (Ed.), Metallography and Microstructures, ASM International, 2004.

[20] D.J. Dyson, K.W. Andrews, Carbide M_7C_3 and its formation in alloy steels, J. Iron Steel Inst. 207 (1969) 208–219.

[21] A. Rouault, P. Herpin, R. Fruchart, Études christallographique des carbures Cr_7C_3 et Mn_7C_3, Ann. Chim. 5 (6) (1970) 461–470.

[22] R. Fruchart, A. Rouault, On the existence of twins in the isomorphous orthorhombic carbides Cr_7C_3, Mn_7C_3, Fe_7C_3, Ann. Chim. Paris 4 (3) (1969) 143–145.

[23] B.H.P.K.V. Brožek, Heptamanganese tricarbide Mn_7C_3, Collect. Czechoslovak Chem. Commun. 48 (10) (1983) 2740–2750.

[24] A. Inoue, T. Masumoto, Carbide reactions ($M_3C \rightarrow M_7C_3 \rightarrow M_{23}C_6 \rightarrow M_6C$) during tempering of rapidly solidified high carbon Cr-W and Cr-Mo steels, Metall. Trans. A 11 (5) (1980) 739–747.

[25] T. Otsuka, H. Hanada, H. Nakashima, K. Sakamoto, M. Hayakawa, K. Hashizume, M. Sugisaki, Observation of hydrogen distribution around non-metallic inclusions in steels with tritium microautoradiography, Fusion Sci. Technol. 48 (1) (2005) 708–711.

[26] G. Kresse, J. Furthmüller, Efficiency of ab-initio total energy calculations for metals and semiconductors using a plane-wave basis set, Comput. Mater. Sci. 6 (1) (1996) 15–50.

[27] G. Kresse, J. Hafner, Ab initio molecular-dynamics simulation of the liquid-metal–amorphous-semiconductor transition in germanium, Phys. Rev. B 49 (20) (1994) 14251–14269.

[28] G. Kresse, D. Joubert, From ultrasoft pseudopotentials to the projector augmented-wave method, Phys. Rev. B 59 (3) (1999) 1758–1775.

[29] J.P. Perdew, K. Burke, M. Ernzerhof, Generalized gradient approximation made simple, Phys. Rev. Lett. 77 (18) (1996) 3865–3868.

[30] A. Jain, S.P. Ong, G. Hautier, W. Chen, W.D. Richards, S. Dacek, S. Cholia, D. Gunter, D. Skinner, G. Ceder, K.A. Persson, Commentary: The materials project: A materials genome approach to accelerating materials innovation, APL Mater. 1 (1) (2013) 011002.

[31] H.J. Monkhorst, J.D. Pack, Special points for Brillouin-zone integrations, Phys. Rev. B 13 (12) (1976) 5188–5192.

[32] W.A. Counts, C. Wolverton, R. Gibala, First-principles energetics of hydrogen traps in α-Fe: Point defects, Acta Mater. 58 (14) (2010) 4730–4741.

[33] G. Henkelman, H. Jónsson, Improved tangent estimate in the nudged elastic band method for finding minimum energy paths and saddle points, J. Chem. Phys. 113 (22) (2000) 9978–9985.

[34] G. Henkelman, B.P. Uberuaga, H. Jónsson, A climbing image nudged elastic band method for finding saddle points and minimum energy paths, J. Chem. Phys. 113 (22) (2000) 9901–9904.

[35] D. Sheppard, G. Henkelman, Paths to which the nudged elastic band converges, J. Comput. Chem. 32 (8) (2011) 1769–1771.

[36] D. Sheppard, P. Xiao, W. Chemelewski, D.D. Johnson, G. Henkelman, A generalized solid-state nudged elastic band method, J. Chem. Phys. 136 (7) (2012) 074103.

[37] D.D. Stefano, M. Mrovec, C. Elsässer, First-principles investigation of quantum mechanical effects on the diffusion of hydrogen in iron and nickel, Phys. Rev. B 92 (2015) 224301.

[38] H. Kimizuka, S. Ogata, M. Shiga, Mechanism of fast lattice diffusion of hydrogen in palladium: interplay of quantum fluctuations and lattice strain, Phys. Rev. B 97 (2018) 014102.

[39] K. Hirata, S. Iikubo, M. Koyama, K. Tsuzaki, H. Ohtani, First-principles study on hydrogen diffusivity in BCC, FCC, and HCP iron, Metall. Mater. Trans. A 49 (2018) 5015.

[40] L. Sun, X. Ji, L. Zhao, W. Zhai, L. Xu, H. Dong, Y. Liu, J. Peng, First principles investigation of binary chromium carbides Cr_7C_3, Cr3C2 and Cr23C6: electronic structures, mechanical properties and thermodynamic properties under pressure, Materials 15 (2022) 558.

[41] V. Vykhodets, O. Nefedova, T. Kurennykh, S. Obukhov, E. Vykhodets, Debye temperature and quantum diffusion of hydrogen in body-centered cubic metals, ACS Omega 7 (2022) 8385.

[42] D. Connétable, Theoretical study on hydrogen solubility and diffusivity in the γ-TiAl L10 structure, Int. J. Hydrogen Energy 44 (2019) 12215.

[43] B. Zhang, J. Su, M. Wang, Z. Liu, Z. Yang, M. Militzer, H. Chen, Atomistic insight into hydrogen trapping at MC/BCC-Fe phase boundaries: the role of local atomic environment, Acta Mater. 208 (2021) 116744.

[44] K.J. Yang, Y.-L. Liu, P. Shao, X. Zhang, Q.-F. Han, Y. Ma, First-principles simulation of h interacting with transition elements in molybdenum for nuclear material application, J. Nucl. Mater. 541 (2020) 152437.

[45] B. Cheng, A.T. Paxton, M. Ceriotti, Hydrogen diffusion and trapping in α-iron: the role of quantum and anharmonic fluctuations, Phys. Rev. Lett. 120 (2018) 225901.

[46] K. Momma, F. Izumi, VESTA: a three-dimensional visualization system for electronic and structural analysis, J. Appl. Crystallogr. 41 (3) (2008) 653–658.

[47] A. Stukowski, Visualization and analysis of atomistic simulation data with OVITO–the Open Visualization Tool, Modelling Simul. Mater. Sci. Eng. 18 (1) (2009) 015012.

[48] M. Audier, P. Bowen, W. Jones, Transmission electron microscopic study of single crystals of Fe_7C_3, J. Cryst. Growth 63 (1) (1983) 125–134.

[49] B. Kaplan, A. Blomqvist, C. Århammar, M. Selleby, S. Norgren, Structural determination of $(Cr, Co)_7C_3$, in: 18th Plansee Seminar, 3–7 June, 2013 in Reutte, Austria, 2013, pp. HM104/1–HM104/12.

[50] J. Paier, M. Marsman, K. Hummer, G. Kresse, I.C. Gerber, J.G. Ángyán, Screened hybrid density functionals applied to solids, J. Chem. Phys. 124 (15) (2006) 154709.

[51] C. Jiang, First-principles study of structural, elastic, and electronic properties of chromium carbides, Appl. Phys. Lett. 92 (4) (2008) 041909.

[52] C.M. Fang, M.A. van Huis, H.W. Zandbergen, Structural, electronic, and magnetic properties of iron carbide Fe_7C_3 phases from first-principles theory, Phys. Rev. B 80 (22) (2009) 224108.

[53] M.A. Konyaeva, N.I. Medvedeva, Electronic structure, magnetic properties, and stability of the binary and ternary carbides $(Fe, Cr)_3C$ and $(Fe, Cr)_7C_3$, Phys. Solid State 51 (10) (2009) 2084.

[54] T.A. Timmerscheidt, P. Dey, D. Bogdanovski, J. Von Appen, T. Hickel, J. Neugebauer, R. Dronskowski, The role of κ-carbides as hydrogen traps in high-Mn steels, Metals 7 (7) (2017) 264.

[55] A. Gross, M. Scheffler, Role of zero-point effects in catalytic reactions involving hydrogen, J. Vac. Sci. Technol. A 15 (3) (1997) 1624–1629.

[56] D.E. Jiang, E.A. Carter, Diffusion of interstitial hydrogen into and through bcc Fe from first principles, Phys. Rev. B 70 (6) (2004) 064102.

Further reading

[1] Y. Wang, T. Hou, Z. Li, H. Lin, X. Yang, G. Wu, D. Zhang, K. Wu, Structure, magnetism, electronic properties and high magnetic-field-induced stability of alloy carbide M_7C_3, J. Magn. Magn. Mater. 538 (2021) 168263.